2020

Effect of O_2 Concentration in Ambient Mixture and Multiphase Radiation on Pollutant Formation in ECN Spray-A

Khaled Mosharraf Mosharraf Mukut
Marquette University

Somesh Roy
Marquette University, somesh.roy@marquette.edu

Combustion Theory and Modelling, Vol. 24, No. 3 (2020): 549-572. DOI.

Effect of O_2 Concentration in Ambient Mixture and Multiphase Radiation on Pollutant Formation in ECN Spray-A

K. M. Mukut
Department of Mechanical Engineering, Marquette University, Milwaukee, Wisconsin
S. P. Roy
Department of Mechanical Engineering, Marquette University, Milwaukee, Wisconsin

ABSTRACT

The present study investigates the formation and evolution of soot and NO_X in a high-pressure constant-volume combustion chamber. This work focuses on the effect of multiphase thermal radiation and O_2 dilution in ambient/exhaust gases, some- times also referred to as exhaust gas recirculation(EGR), qualitatively and quantitatively. The spray-A case (n-dodecane as fuel) from Engine Combustion Network (ECN) is used as the target condition. Two different soot modeling approaches have been considered: a semi-empirical two-equation model and a detailed method of moments with interpolative closure (MOMIC) model. A multiphase photon Monte Carlo (PMC) solver with line-by-line (LBL) spectral data is used to resolve radiative heat transfer. Results

show that effect of radiation on soot is minimal in spray-A. Inclusion of radiation modeling, on the other hand, marginally reduce NO prediction. Both peak soot and NO formation increases with O_2 content in the ambient gas. Oxygen content in ambient gas is also found to have significant effect on soot sizes as the mean soot diameter increases along with considerable widening of the diameter distribution with the increase of O_2 percentage in the ambient gas.

KEYWORDS

ECN; Radiation; EGR; Soot; NO_X

1. Introduction

Internal combustion engines play an important role in transportation and power generation sectors. Combustion processes are often accompanied by large amount of harmful emissions like soot and NO_X. Therefore, it is very important to understand the outcomes of combustion processes and to be able to predict the effect of different operating conditions typically found in internal combustion engines. Reducing the amount of pollutant formation while keeping the engine efficiency unaffected has been a topic of great interest among the engine researchers in recent decades. Exhaust gas recirculaiton (EGR) is often used to reduce the NO_X emission in modern internal combustion engines. Use of EGR dilutes the O_2 concentration which results in a lower flame temperature in the combustion chamber [1, 2]. Addition of EGR in diesel engines tends to increase soot formation which results in an increase in radiative heat loss from soot [3].

The presence of high pressure and temperature along with spray and particulate matters make the combustion dynamics very complex in internal combustion engines. The complex multiphysics interaction makes it further difficult to understand and model the fundamental processes in engine-relevant conditions. Although the radiative heat transfer can contribute 12%-15.5% of the total thermal heat loss [4, 5] in different configurations, radiation modeling is often neglected or simplified in engine simulations.

The present work focuses on numerical modeling of high-pressure, constant volume spray combustion experiments reported by engine combustion network (ECN) [6]. Liquid n-dodecane spray (ECN spray-A) is used as the fuel and different extent of O_2 dilution configurations are considered. A series of previous studies have been con- ducted on ECN spray-A case. Som et al. [7] studied several ECN combustion chamber and proposed baseline parameters for the numerical approach to model those cases. Fernandez et al. [8] used a transported probability density function (TPDF) solver to investigate the soot formation in ECN spray-A case. To resolve the turbulence radiation interaction (TRI) properly they used a photon Monte Carlo/line-by-line (PMC/LBL) radiation solver. However, the radiation solver was not coupled with the gas phase chemistry for all simulations in that study and the effect of O_2 dilution of the ambient gases was not investigated. Haworth and coworkers [9, 10] reported that nongray radiation contributes not only to the wall heat loss but also in the spatial redistribution of temperature. Chishty et al. [11] also studied the importance of radiative heat transfer using three different radiation model for spray-A and concluded that the effect of turbulence radiation interaction (TRI) is important and it increases the overall radiation emission. Recently, they also investigated the soot formation in spray-A case with turbulent chemistry interaction (TCI) [12]. They used a two-equation semi-empirical soot model and assumed an optically thin radiative heat transfer configuration. However, due the presence of high pressure inside the combustion chamber, the optically thin approximation does not hold true [8]. In another recent study, Yue and Reitz [13] used a discrete ordinate method (DOM) to study the effect of radiative heat transfer on soot and NO_X formation and reported that, radiation can influence the engine-out soot production by as much as 50% under certain conditions.

Although different numerical studies have been conducted regarding TCI, gas phase radiation and spray radiation individually, to the best of our knowledge, no study has been conducted yet coupling the multiphase radiation with soot models in spray-A spray combustion cases. As some researchers have pointed out, including spray droplets in radiation transfer may have some effect on pollutant formation under certain conditions [14, 15]. In this work, we systematically investigate the effect of multiphase radiation, soot model sensitivity and different extent of oxygen dilution on pollutant production in ECN spray-A case.

A Reynolds average simulation framework is used along with a photon Monte Carlo line by line (PMC/LBL) detailed multiphase radiation solver. Both spray and gas phase radiation is studied in depth for different O_2 dilution configurations and their effect on soot and NO_X formation. The soot formation and distribution is studied in details using a detailed method of moment soot model. The novelty of the present study lies in the systematic study of the local and global effects of both spray and gas phase radiation under the influence of different O_2 dilution configurations, and detailed investigation of soot characteristics and size statistics at different stages of combustion.

2. Target cases

The ECN spray-A configuration is an optically accessible constant volume spray combustion chamber with a volume of 1147 cm3. A wide range of data for different levels of O_2 in the ambient gas is reported by ECN. The desired initial ambient configuration is achieved by pre-burning a premixed acetylene (C2H2) mixture. A more detailed description is available at [16].

The present study considers spray-A configuration for three different initial oxygen percentages (13%, 15% and 21%) at an initial temperature of 900 K. The X% (where, X= 13, 15 or 21) initial oxygen configuration indicates the amount of oxygen present in the ambient gas mixture. The ambient gas mixture is derived from the premixed burning of the acetylene mixture. The product of the preburn mixture is emulating the EGR configurations. It should be noted that, for constant volume combustion chamber this kind of mixture is often referred to as oxidizer dilution. The initial ambient density is 22.8 kg/m3 and internal pressure is 6 MPa. The injection pressure is 150 MPa and injector orifice diameter is 90 μm. The injection duration is 6 ms. For the non-reacting cases, a 0% O_2 configuration (mixture of only ambient gases and nitrogen but no O_2) is considered while for the reacting cases, the recommended percentages of nitrogen (N2), water (H2O) and carbon-di-oxide (C O_2) with different oxygen (O_2) quantities are considered as provided in [17]. The liquid and vapor penetration lengths for non- reacting case and lift-off-length (LOL) & ignition delay (ID) for reacting cases are used for model validation.

3. Numerical methodology

The turbulent flow field is modeled using an unsteady Reynolds-averaged Navier- Stokes (URANS) [18] approach using OpenFOAM-2.3.x CFD toolbox [19]. A pressure- based finite-volume method is used to solve the coupled pressure, momentum, and energy equations with second-order spatial discretization. The baseline model parameters used in the present study are summarized in Table 1. Although TCI and TRI effects can be important in these configurations, accurate modeling of these effects requires a computationally expensive probability density function (PDF) approach. Therefore, it is prudent to evaluate global effects of multiphase radiation and O_2 dilution before a computationally expensive combination of detailed models (e.g., PDF/MOMIC/PMC/LBL) can be selected to explore more details of specific cases. Considering the number of detailed simulations to be performed in this work, a PDF approach with parametric sweep, as done in the current work, would add a huge computational burden. Therefore, as a first order estimate, effects of TCI and TRI are not considered in the simulations. Even without the TCI and TRI effects, the qualitative trends seen in this work are expected to be

useful. Based on these trends a select number of cases and model combinations can be used with an accurate TCI/TRI model to further investigate these configurations.

The two-equation *k E* turbulence model is used in the present study. The C_d1 constant is increased from 1.44 to 1.55 as recommended by [20]. The liquid spray is modeled using stochastic Lagrangian-parcel method [21]. The liquid penetration length is dependent on the spray break-up model. Reitz-Diwakar secondary break- up model [22] is used in the current study. The striping constant, C_s, used in the secondary break-up model is set to match the numerical liquid penetration length with the experimental results (C_s = 9.0). The vapor penetration length is dependent on the initial turbulence condition. The initial *k* and *E* values are chosen to match the experimental vapor penetration length.

A 54-species, 269-reaction skeletal n-dodecane ($C_{12}H_{26}$) mechanism developed by Yao et al. [23] is used in this study. This mechanism was previously used by Fernandez et al. [8] who showed reasonable agreement with the experimental data. For NO formation, the thermal NO pathways following extended Zeldovich mechanism are added to the mechanism [24–26]. Two different soot models are used in the present study: a semi-empirical two-equation model [27] and method of moments with interpolative closure (MOMIC)[28]. The two-equation model solves two transport equations for soot mass fraction and particle number density. Soot formation is semi-empirically linked with C_2H_2, whereas the soot oxidation pathways include O_2. On the other hand, MOMIC is a detailed soot model which solves for a finite number of moments of the particle size distribution function (PSDF) by solving a population balance equation. This model can provide more information about the soot size distribution. MOMIC is expected to provide better estimation of soot formation when used with a sufficiently accurate and detailed chemical mechanism [29]. The soot surface growth in MOMIC follows hydrogen abstraction C_2H_2 addition (HACA) pathways [30–34]. Soot oxidation takes place due to reaction with O_2 and OH. The details of the models can be found in [28, 35]. In this work we used first six moments for MOMIC formulation. Additionally, since the chemical mechanism used does not contain any polycyclic aromatic hydrocarbon (PAH) we used an acetylene-based nucleation scheme for MOMIC [36].

A fully coupled spectral photon Monte Carlo (PMC) radiation solver [14, 37, 38] is used in the present study to account for the gas phase radiation. In PMC, radiation exchange is solved by emitting and tracing a large number of photon bundles or rays. The radiative properties are calculated using a line-by-line (LBL) spectral database obtained from HITEMP2010 database [39]. Three gaseous species (H_2O, CO and CO_2) and soot are considered as participating species. The radiative properties of the soot particles are calculated using a wavenumber-dependent formulation [40]. Spray-phase radiation is based on the multiphase radiation model developed by Roy et al. [14]. The spray droplets are much cooler than surrounding gases and thus considered non- emitting. Due to lack of spectrally-resolved radiative property data for dodecane, a gray (i.e., constant complex index of refraction, *n ik*) assumption is applied to spray droplets. Tuntomo [41] studied the complex index of refraction of n-heptane and n-decane for the mid-infrared range (2-10 μm) and concluded that the refractive index (*n*) varies by a little while the index of absorption (*k*) varies wildly with wavelength. In the later studies these outcomes are confirmed by Dombrovsky [42, 43] and the complex index of refraction for Diesel fuel was found to be *n* O(1.5) and *k* O(10^{-4}– 10^{-1}) for the mid-infrared range. Following an earlier work [14], the values of the complex index of refraction of the fuel droplets is assumed to be constant at *n*=1.5 and *k*= 0.002 in the present study. Scattering by spray droplets has also been neglected as it was shown to have negligible effect [14].

Many of the numerical models are same as what has been used and validated by Fernandez et al [8]. However, this is the first work to couple a multiphase PMC/LBL approach with the chemistry in this configuration. Additionally, while the previous work [8] focused on the effect of TCI/TRI and spectral radiation, this work focuses on effect of soot model, coupled radiation, and O_2 percentage in ambient gas on soot and NO_X production. As done in [8], a two-dimensional axisymmetric computational domain with a 5° wedge [8] (1/72th of the experimental domain) is considered as the reaction vessel. The axial and radial dimensions are

respectively 108 mm and 58 mm. The entire domain is divided into 12,800 non-uniformly distributed cells. The minimum grid size is approximately 0.25 mm. The simulation domain is bounded by three walls and two symmetric boundaries. The spray is injected from the corner of the simulation domain. The injection pressure is 150 MPa and the mass flow rate is adjusted to match with the $1/72^{th}$ of the experimental domain. The injector diameter is 90 µm and co-efficient of discharge is set to 0.89 as per ECN recommendation. Rosin-Rammler distribution [44] is used to control the size distribution of the spray parcels introduced in the simulation domain. Standard wall function is used as the wall boundary conditions. The recommended spray injection rates provided by ECN are used throughout this study. The computational time step is set at $5 \times 10^{-}7$ s.

4. Results and discussions

As mentioned earlier, the numerical model parameters (summarized in Table 1) are tuned to match with the experimental liquid and vapor penetration lengths. Since the simulations involve several models, all of which has several tunable parameters, it is impractical to tune each of these models to match each experiment on a case-by-case basis. Therefore, we restricted tuning to only reference nonreacting data such as penetration lengths. Once the tuning is achieved, the parameters are fixed for the rest of the study. We then further validated the choice of parameters by comparing simulation results with different reacting characteristics such as the ignition delay (ID), lift-off-length (LOL), heat release rate, pressure rise etc. Here we only show validation plots for ID and LOL for brevity.

4.1 Non-reacting validation: Penetration length

In the non-reacting cases, fuel spray is injected in the chamber filled with only the ambient gases without any oxygen. ECN defines liquid penetration length as the distance from the nozzle, at which the liquid fuel mass fraction becomes 1%. On the other hand, the vapor penetration length is the distance from nozzle at which the fuel mass fraction becomes 0.1%. Since there is no reaction involved (due to the absence of oxygen), the penetration lengths are only affected by the spray break-up parameters and the turbulent mixing configurations. The experiments use acetylene (C2H2) pre- mixed combustion to attain the initial conditions required for the self-ignition of the spray. The constant-volume acetylene preburn creates a decaying turbulence field, that serves as the intial condition for the spray injection. The vapor penetration length is affected mostly by this initial turbulence field. Therefore, the initial turbulence levels (k and E) are adjusted to match the experimental vapor penetration length. The C_E1 parameter affects both vapor penetration length and lift-off-length (LOL) as discussed in later section. Figure 1 compares the liquid and vapor penetration length obtained from the experiments and simulations.

4.2. Reacting validation: Ignition delay (ID) and lift-off-length (LOL)

There are several ways to define the ignition delay in a spray combustion system. In this study, a pressure based ignition delay (ID) definition approach is adopted [45, 46]. Accordingly, the ignition delay (ID) period is defined as the instance at which the average pressure in the combustion chamber increases by a nominal 3 kPa amount. This instance indicates the beginning of the second stage of combustion. The chemical heat release rate (HRR) is maximum at this point. Figure 2a depicts the ignition delay (ID) for different O_2 percentage cases at 900 K. The numerical data follows the same trend as the experiments and the curves are parallel to each other. The ignition delay (ID) period decreases with the increase in O_2 quantity.

The change in the lift-off-length (LOL) with oxygen percentage is shown in Fig. 2b. The lift-off-length (LOL) is defined as axial location in the quasi-stationary flame where the OH mass fraction becomes 14% of the maximum value in the whole do- main. The quasi-stationary flame quantities are obtained by temporal averaging the scalars. In this study, as done by Bolla et al. [47], it is assumed that the reaction domain achieved the quasi-stationary state at 5 ms from the start of injection (SOI). Just like the ignition delay (ID), the lift-off-

length (LOL) also decreases with the in- creasing O_2 quantity. The numerical LOL profiles also follow the experimental LOL profiles qualitatively. The present trends in results are in agreement with similar study conducted by Fernandez et al. [8].

The discrepancy in the ignition delay (ID) results between the experiments and the numerical simulation can be explained in terms of the choice of chemical mechanism and TCI. As mentioned earlier, the TCI effects are not considered in the present study as we used a partially stirred combustion model. Usually an over-prediction of both ignition delay (ID) and lift-off-length (LOL) occurs when TCI is ignored [47– 49]. Mukut and Roy [50] also showed that choice of chemical kinetic mechanism can significantly alter the flame lift off length (LOL).

The lift-off-length (LOL) also depends strongly on the turbulence characteristics inside the simulation domain. As discussed earlier, the C_E1 parameter in the *k E* turbulence model was changed to 1.55 to match the experimental vapor penetration length. However, this modification increases the lift-of-length. The consistent over- prediction of the LOL is attributed to the limitations of the turbulence model including the absence of TCI modeling [47–49] as well as chemical mechanism [50].

4.3. Effect of radiation

In this work the gas phase radiation and the spray phase radiation are considered separately. Radiation of the gas phase species and spray droplets may have some effect on pollutant formation behavior due to the local change in temperature because of radiative heat loss. The inclusion of radiation modeling usually results in lowering of temperature and pressure. Both the average temperature and pressure decreases with decreasing O_2 percentage in the ambient gases during the injection period. But, after the injection ends, the rate of cooling increases with higher O_2 percentage.

Radiation may not noticeably affect the global quantities but it may affect the combustion dynamics by redistributing the temperature field in the simulation domain. The wall emission can also play an important role in near-wall temperature distribution. This change in the temperature field may affect the formation of soot and NO_X throughout the domain. To identify the effect of radiation from different phases (gas and spray), three sets of simulations were performed – without radiation, with only gas-phase radiation (i.e., spray is not participating in radiation), and with both gas and spray-phase radiation (i.e., C O_2, H2O, CO, soot and spray droplets are all participating in radiation heat transfer). As a representative case, 21% O_2 case with MOMIC soot model is discussed here in details. The trends observed are same for other cases.

Figures 3a–c show the difference in temperature distribution in the simulation domain due to different treatments of radiation at three different instances of time (2 ms, 5 ms and 7 ms) and Fig. 3d shows the temperature contours with and without radiation models at 5 ms. Noticeable local differences in temperature are observed in these figures due to the multi-phase radiation. A point to note here is that the alternating hot and cold layers seen in the difference plots (Figs. 3a–c) are because of minor shifts in flame front between one simulation and another due to randomness in radiation and spray models and should be ignored while making any inference. In general, gas- only radiation cools down the flame slightly (e.g., mostly hotter regions in Fig. 3c). However, presence of spray in radiation model makes things highly complex. Direct radiative heating of spray droplets was found to be negligible compared to convective heating due to high injection pressure. This is in agreement with earlier findings [14]. Although spray droplets are not expected to be heated up directly by radiation in any significant amount, their presence may alter local temperature slightly [14]. Presence of hotter region near the downstream wall at around 5 ms in Figs. 3a, 3b and 3c indicates that the inclusion of spray in radiation may make the flame marginally shorter, possibly due to localized cooling of gases near the nozzle upstream of the flame. Figure 3b also indicates that the inclusion spray in radiation makes the flame marginally

wider, but also marginally cooler at core post-injection (at 7 ms). It must be noted here that the difference in temperature due to radiation is very localized and small in magnitude, and therefore it does not affect the volume-averaged temperature noticeably. As a global quantity for radiation, the share of radiative heat transfer to the wall compared to the chemical heat release (HRR) (radiant fraction) was also calculated. At around 5 ms (quasi steady state), the radiant fraction for the 13%, 15%, and 21% O_2 configurations were, respectively, 2.1%, 2.2%, and 2.8%.

4.3.1. Soot

Two soot models have been used in this study: a two-equation semi-empirical model and a method of moment of interpolative closure (MOMIC). Figure 4 depicts the evolution of soot volume fraction contour with different soot models for 21% O_2 case with gas phase radiation at 5 ms. The location and spread of soot formation shows qualitative agreement.

ECN [6] provides the global soot production data with time within an experimental field of view (17.2 mm to 67.2 mm in the axial direction). Figure 5 compares the temporal evolution of total soot mass with the experimental data within the experimental field of view for both soot models. MOMIC was run without any tuning or optimization and results show overprediction of total soot mass in 21% O_2 case. As reported later (Sec. 4.4.1), the MOMIC results match well in 15% and underpredicts in 13% O_2 cases. The sensitivity of the two soot models with initial amount of O_2 in the ambient mixture varies significantly and is discussed later in Sec. 4.4.1.

From Fig. 3, we have seen the effect of spray and gas-phase radiation on the local temperature distribution. Since soot formation is sensitive to the temperature distribution, difference in radiation treatments may affect the overall soot formation. The soot volume fraction contours for the 21% case with and without spray and gas phase radiation at 5 ms are shown in Fig. 6. It is interesting to see that the overall soot production zone remains almost (a marginal reduction can be seen with spray- and gas-phase radiation) same with or without radiation considerations. This is possibly because of the small magnitude of the temperature difference in the soot formation zones. The effect of spray- and gas-phase radiation remains minimal across all the O_2 percentage cases as seen from the global soot production plots in Fig. 7. This result is in agreement with the contemporary studies [11, 13].

4.3.2. NO_X

Apart from soot particles, NO_X is another major source of pollutant in internal combustion engines. NO being a major constituent of NO_X, we treat NO as an indicator of overall NO_X behavior in this study. The present study considers only thermal NO production. In general, NO formation is a strong function of temperature and mixture fraction but has a weak correlation to pressure inside the combustion chamber [51]. Because of the change in temperature distribution due to the addition of radiation model, NO_X production is affected.

Figure 8 demonstrates when and how spray-phase radiation and gas-phase radiation influence NO mass fraction inside the simulation domain. The effect of spray-phase radiation is small compared to gas-phase radiation. The effect of spray-phase radiation decreases after the end of injection as observed in Fig. 8c. On the other hand, the gas phase radiation dominates the core segment of the flame and near the wall. The effect of gas-phase radiation become more dominant with time specially near the wall. From Fig. 8, it is evident that, the wall heat transfer plays an important role in NO formation. With the inclusion of radiation model, temperature near the wall decreases due to radiative cooling, leading to a decrease in NO production.

The localized cooling effect observed with the inclusion of radiation restricts NO formation slightly. Figure 9 demonstrates how the global NO production changes with time due to radiation in 21% O_2 case. Gas phase radiation plays slightly more important role in reducing the amount of NO (almost 5%) than the spray phase radiation for which the effect is not as impactful as the gas phase radiation (3.2%).

4.4. Effect of O_2 quantity in ambient gases

Reduction of O_2 quantity in ambient gases results in a reduction of temperature which helps reducing NO_X emissions. However, in terms of soot, things are a little different. The increase of O_2 helps increasing the soot formation but also increases the soot oxidation rate. The link between the amount of O_2 in the ambient gas and soot emission is therefore not quite linear.

4.4.1. Soot

As discussed earlier, two different soot models have been employed in the current study. Figure 10 depicts the effect of O_2 percentage in the ambient gas on soot formation behavior across both soot models at 5 ms (considering quasi-steady flame) and experimental quasi-steady soot volume fraction. Both soot models show qualitative agreement with the experimental results. However, the MOMIC tends to over-predict the amount of soot for higher O_2 percentage cases and under-predict at lower O_2 percentage cases. Both the location and the amount of soot production are affected by the O_2 percentage in the initial ambient mixture. The location of the peak soot volume fraction moves away from the injection nozzle with the decrease of the O_2 per- centage in the ambient mixture. Also, a steady increase in peak soot volume fraction is observed with the increase of O_2 percentage.

Figure 11 depicts the effect of O_2 percentages in the initial ambient mixture and different soot models on global soot formation. The results are also compared with the experimental soot data provided by ECN. Although, the two-equation and MOMIC soot model shows qualitative agreement in soot volume fraction profile as discussed in Figure 10, there is significant quantitative difference between the soot models. The semi-empirical two-equation model shows surprisingly consistent agreement with experimental data in all cases studied but MOMIC seems to be very sensitive towards the amount of O_2 in the ambient gases. O_2 plays an important role in the surface growth during soot formation [32, 52] as well as in oxidation of soot particles. The sensitivity of the MOMIC with O_2 percentage in the ambient gases can be partially attributed to this two-way role of oxygen and the importance of surface growth in MOMIC. The correlations used in the semi-empirical two-equation model lump these processes together. Two-equation model has been previously shown to be less sensitive to small differences in chemical mechanisms and local equivalence ratio [29, 35, 53, 54]. In the current study also, this model is found to be less sensitive to O_2 percentage in the ambient mixture than MOMIC. MOMIC has been shown to be more sensitive to gas-phase chemistry and equivalence ratio than semi-empirical model [29, 35]. Additionally, MOMIC results are also sensitive to model parameters such as different variants of HACA mechanism and “steric factor” formulation [29, 55], particularly when surface growth is a dominant process. In this study we did not perform any optimization of these model parameters and chemical mechanisms. This can contribute to the large variations in MOMIC results across different O_2 dilutions. It should be noted that, the good match with experimental data for all three O_2 dilution cases from the semi-empirical model is somewhat surprising and does not necessarily indicate that two-equation model is a better soot model than MOMIC. With TCI effects considered, along with a better chemistry with aromatics, MOMIC has been shown to produce a better match in Spray-A in the literature [8]. This observation also supports the conclusion that the accuracy of detailed soot models depends strongly on model parameters as well as other aspects such as the chemical mechanism, turbulence- chemistry interaction models, etc [8, 29, 56].

4.4.2. NO_X

As discussed earlier NO formation is very strongly related to the temperature and mixture fraction of the flame in the combustion chamber[51]. As the O_2 % in the ambient gas mixture decreases, the temperature inside the combustion chamber also decreases and so does NO. Figure 12 depicts the change in the temperature contours inside the combustion chamber due to the change in the initial O_2 quantity in the ambient mixture. The temperature rises as the O_2 percentage in the initial ambient gas mixture increases. This rise in temperature is

significant when the O_2 quantity increases from 15% to 21% in the ambient mixture. This large change in temperature is also reflected in the change in NO production at high O_2 content as seen from Figure 13.

Figure 13 illustrates the comparison of NO formation behavior with different O_2 percentage cases at 5 ms. The maximum value in the contour plots are kept same as the maximum NO mass fraction in individual cases. From 13% to 15% O_2 case, the peak NO mass fraction increases by an order of magnitude. Two orders of magnitude increase is seen between 21% and 15% O_2 content. With the decrease in the O_2 content, the wall radiative heat transfer effects can also be observed. The NO profiles for 13% O_2 case is much wider than the 21% case near the wall. The global effect of the initial O_2 percentages on overall NO production is shown in Figure 14. The total NO mass produced in 21% O_2 case is much higher than the other two. Figure 14 clearly indicates that the NO emission can be significantly reduced with the lowering of O_2 in the ambient mixture.

4.5. Soot size statistics

The size and morphology of the engine-out soot have significant effect on the environment. The effect of initial ambient O_2 concentration and radiation on global soot yield has been described in the previous sections using both a two-equation model and a MOMIC soot model. The semi-empirical two-equation soot model does not resolve size-related information in great detail. MOMIC, on the other hand, follows evolution of soot from first principle and can resolve the moments of the PSDF. MOMIC accounts for four fundamental physio-chemical processes involving soot – nucleation, coagulation, surface growth (following the HACA [30] pathway), and oxidation [e.g., see 28, 29, 32, etc. for details]. In this section, we present some global information related to the soot particle size distribution obtained from MOMIC. It is important to note here that, the current MOMIC formulation assumes spherical soot particles and the gas-phase chemical mechanism does not contain any PAH. Therefore, the analysis presented here may lack some details in soot morphological information. But the information extracted are still worth looking as they reveal some important qualitative information.

Figure 15 depicts the global probability density function (PDF) of the soot particle diameters in different initial O_2 configurations considering the entire chamber at 5 ms. It is evident that the diameter distribution becomes wider with the increase of O_2 percentage in the ambient mixture. The presence of more O_2 in the ambient mixture invokes a more suitable condition for the surface reaction which accelerates surface growth. Thus, we get soot particles with larger diameter in higher O_2 cases. The 21% O_2 almost doubles the soot diameter compared to 15% O_2 case.

The evolution of the diameter of the soot particles with time also gives us important insights about the evolution of soot. In the cases under consideration, the simulation is run for 10 ms while the spray lasts for 6 ms. Figures 16 – 18 show the changes of diameter PDF with time inside the combustion chamber for 13%, 15% and 21% O_2 cases respectively. For clarity, the plots are divided into two separate parts, (a) during spray injection and (b) after the end of spray injection. The total soot mass and number density in the simulation domain on a particular time is also included in the corresponding legends. The bimodal nature of the PDF profiles show the balance between formation, coagulation, surface growth, and oxidation during different phases of combustion. Only nucleation and coagulation affect the number density of soot – nucleation introduces incipient soot particles, whereas coagulation reduces number of soot particles without affecting soot mass. On the other hand nucleation and surface growth introduce new mass to soot, while oxidation reduces mass of a soot particle. The first peak is indicative of mostly the incipient soot particles. The second peak represents the previously formed soot particles which are going through a balance be- tween coagulation, surface growth and oxidation. Depending on the extent of different phases of soot formation, the shape of the diameter PDF can change and because of that, the width and existence of the two peaks may also vary.

During the spray injection, all the cases under consideration show a rapid increase of soot mass and number initially up to 2 ms as seen from Figs. 16a, 17a and 18a. This indicates rapid nucleation in the beginning of each

case. After that, the total number of soot particles becomes more or less steady until the end of spray injection. During this period the soot mass continues to increase. This increase in soot mass with a small change in total number of soot particles represents rapid surface growth during this period. The soot diameter PDFs keep getting wider until a balance between surface growth and oxidation kicks in. After the end of spray injection, the amount of soot decreases rapidly due to oxidation as seen from Figs. 16b, 17b and 18b. The effect of nucleation increases with the decrease of O_2 percentage in the combustion domain. For the 13% O_2 case there is essentially one single peak that is visible during the entire 10 ms. Although the diameter profile widens from 3 ms to up to 8 ms due to coagulation and surface growth, these phenomena are not strong enough to produce a distinct second peak. The peak of the PDF remains close to 2 nm indicating strong effect of nucleation during initial stage (up to 2 ms) and oxidation during the later stage (8 ms to 10 ms). For 15% O_2 cases, we see a co-existence of both mature (larger diameter) and newly-formed (smaller diameter) soot particles even after the injection ends at 6 ms (until 7 ms). The presence of a second peak indicates increasing importance of surface growth and coagulation. For 21% O_2 case, the bimodal shape is only visible during initial stage (up to 2 ms). Beyond that the surface growth essentially shifts the peak towards larger particles (2 ms to 5 ms). The oxidation is strongest in this case resulting in quick elimination of large particles immediately after the end of injection (Fig. 18b). All cases show a very similar soot diameter PDF between 9 ms and 10 ms which indicates a slow-down of physio-chemical activities related soot. This is because by this time most of the soot has oxidized from the domain as also seen in Fig. 7. From Figures 17 and 18 we observe two distinct trend with time. In the first half, coagulation and surface growth becomes dominant over soot nucleation as seen by shift of diameters to larger values. In the later half, oxidation becomes more prominent over surface growth as seen by a decrease in larger diameter particles. This eventually decreases the diameter of soot particle and produces a narrow diameter PDF with time.

The axial variation of the soot diameter gives us important insights about the maturity of the soot particles along the direction of the spray. Figure 19 depicts the axial variation of the spatially-averaged (along the horizontal plane) diameter PDF in 21% O_2 configuration at three different axial locations (36 mm, 45 mm and 60 mm). The colored dots in the plot represent the planar mean of soot diameter at these locations. The legend contains the experimentally planar mean of soot diameter as measured by Cenker et al. [57] at these locations. The numerical planar-averaged diameter is within 30% of experimental data of the experimental data. The locations are chosen to represent different segments of the soot formation zone. The 36 mm location marks the start of the soot formation zone and 60 mm location represents the peak soot formation zone as seen in Figure 6. The bimodal nature of the diameter PDFs are more pronounced in the downstream than the upstream locations. The magnitude of the peaks decrease and the shape of the profiles shifts towards larger particles at the 60 mm location. This points to the dominance of surface growth and coagulation at this location.

5. Conclusions

A comprehensive numerical study has been conducted on ECN spray-A combustion chamber with detailed chemistry, detailed radiation solver, and different soot models for different initial O_2 concentration in the ambient mixture. The numerical results are validated with liquid penetration length, vapor penetration length, ignition delay (ID), lift-off-length (LOL), and global soot mass. The soot and NO_X formation behaviors are carefully investigated to see how they change with radiation and initial O_2 configurations. The soot diameter distributions are also examined and compared with the experimental data. Some key observations of the present study are stated below.

- The effect of radiation is negligible on the average temperature and pressure of the spray-A combustion chamber.
- Effect of spray and gas phase radiation on soot is minimal in ECN spray-A combustion chamber.

- As O_2 percentage in the ambient mixture increases, the peak soot volume fraction also increases.
- MOMIC shows significant sensitivity towards the O_2 concentration.
- Both Radiation and amount of O_2 has noticeable effect on NO production. In- crease in O_2 percentage increases NO. Radiation causes change in local temperature distribution, which in turn reduce NO production throughout the domain.
- The gas-phase radiation has more effect on NO formation than the spray-phase radiation.
- Both location and diameter distribution of the soot particles are affected by the initial O_2 percentage in the ambient mixture. The mean soot diameter increases with increase in O_2 percentage.
- The diameter distribution becomes wider with the increase of oxygen percentage in ambient mixture. Surface growth and coagulation becomes dominant down- stream, away from the nozzle. Oxidation starts to dominate after the end of spray injection.

6. Acknowledgement

Part of this work used the Extreme Science and Engineering Discovery Environment (XSEDE) [58], which is supported by National Science Foundation grant number ACI- 1548562. The XSEDE system “comet” at the San Diego Supercomputer Center at UC San Diego was utilized for some simulations through allocation ENG170021.

References

1. N. Ladommatos, S.M. Abdelhalim, H. Zhao, and Z. Hu, The dilution, chemical, and thermal effects of exhaust gas recirculation on diesel engine emissions - part 4 : Effects of carbon dioxide and water vapour, SAE Tech. Pap (1997), p. 961167, Available at http://dx.doi.org/10.4271/971660.
2. N. Ladommatos, S.M. Abdelhalim, H. Zhao, and Z. Hu, Effects of EGR on heat release in diesel combustion, SAE Technical Paper (1998), p. 980184, Available at http://dx. doi.org/10.4271/980184.
3. R. Egnell, The influence of EGR on heat release rate and NO formation in a DI diesel engine, SAE Technical Paper (2000), pp. 2000–01–1807, Available at https://doi.org/ 10.4271/2000-01-1807.
4. J. Abraham and V. Magi, Modeling radiant heat loss characteristics in a diesel engine, SAE Technical Papers (1997), p. 970888.
5. J. Abraham and V. Magi, Application of the discrete ordinates method to compute radiant heat loss in a diesel engine, Numerical Heat Transfer, Part A: Applications 31 (1997), pp. 597–610.
6. Engine Combustion Network. Available at https://ecn.sandia.gov.
7. S. Som, G. D’Errico, D. Longman, and T. Lucchini, Comparison and standardization of numerical approaches for the prediction of non-reacting and reacting diesel sprays, SAE Technical Paper (2012), pp. 2012–01–1263, Available at https://doi.org/10.4271/ 2012-01-1263.
8. S.F. Fernandez, C. Paul, A. Sircar, A. Imren, D. Haworth, S. Roy, and M. Modest, Soot and spectral radiation modeling for high-pressure turbulent spray flames, Combustion and Flame 190 (2018), pp. 402–415.
9. D.C. Haworth, C. Paul, A. Sircar, A. Imren, S.P. Roy, W. Ge, and M.F. Modest, Soot and Spectral Radiation Modeling in ECN Spray A and in Engines, in International Multidimensional Engine Modeling User’s Group Meeting at the SAE Congress, Detroit, MI. 2017.
10. C. Paul, S. Ferreyro Fernandez, D.C. Haworth, S. Roy, and M.F. Modest, A detailed modeling study of radiative heat transfer in a heavy-duty diesel engine, Combustion and Flame 200 (2019), pp. 325–341.
11. M.A. Chishty, M. Bolla, E. Hawkes, Y. Pei, and S. Kook, Assessing the importance of radiative heat transfer for ECN Spray A using the transported PDF method, SAE International Journal of Fuels and Lubricants 9 (2016), pp. 2016–01–0857, Available at https://doi.org/10.4271/2016-01-0857.
12. M.A. Chishty, M. Bolla, E.R. Hawkes, Y. Pei, and S. Kook, Soot formation modelling for n-dodecane sprays using the transported PDF model, Combustion and Flame 192 (2018), pp. 101–119.
13. Z. Yue and R.D. Reitz, Numerical investigation of radiative heat transfer in internal combustion engines, Applied Energy 235 (2019), pp. 147–163.

14. S.P. Roy, J. Cai, and M.F. Modest, Development of a multiphase photon Monte Carlo method for spray combustion and its application in high-pressure conditions, International Journal of Heat and Mass Transfer 115 (2017), pp. 453–466.
15. H. Watanabe, R. Kurose, S. Komori, and H. Pitsch, Effects of radiation on spray flame characteristics and soot formation, Combustion and Flame 152 (2008), pp. 2–13.
16. L.M. Pickett, C.L. Genzale, G. Bruneaux, L.M. Malbec, L. Hermant, C. Christiansen, and J. Schramm, Comparison of diesel spray combustion in different high-temperature, high-pressure facilities, SAE International Journal of Engines 3 (2010), pp. 2010–01–2106, Available at https://doi.org/10.4271/2010-01-2106.
17. Engine Combustion Network, Ambient configuration. Available at https://ecn.sandia.gov/diesel-spray-combustion/sandia-cv/ambient-conditions/.
18. S. El Tahry, k-epsilon equation for compressible reciprocating engine flows, Journal of Energy 7 (1983), pp. 345–353.
19. OpenFOAM 2.3.X CFD Toolbox. Available at http://www.openfoam.org.
20. S. James, M.S. Anand, M.K. Razdan, and S.B. Pope, In situ detailed chemistry calcula- tions in combustor flow analyses, Journal of Engineering for Gas Turbines and Power 123 (2001), p. 747, Available at https://doi.org/10.1115/1.1384878.
21. J.K. Dukowicz, A particle-fluid numerical model for liquid sprays, Journal of Computational Physics 35 (1980), pp. 229–253.
22. R.D. Reitz, Modeling atomization processes in high-pressure vaporizing sprays, Atomization and Sprays 3 (1987), pp. 309–337.
23. T. Yao, Y. Pei, B.J. Zhong, S. Som, T. Lu, and K.H. Luo, A compact skeletal mechanism for n-dodecane with optimized semi-global low-temperature chemistry for diesel engine simulations, Fuel 191 (2017), pp. 339–349.
24. Y.B. Zeldovich, P.Y. Sadovnikov, and D. Frank-Kamenetskii, Oxidation of nitrogen in combustion, translation by M. Shelef, Academy of Sciences of USSR, Institute of Chemical Physics, Moscow-Leningrad (1947).
25. G.A. Lavoie, J.B. Heywood, and J.C. Keck, Experimental and theoretical study of nitric oxide formation in internal combustion engines, Combust. Sci. Technol. 1 (1970), pp. 313–326.
26. V. Raj Mohan, Development and application of a transported probability density function model for advanced compression-ignition engines, Ph.D. diss., The Pennsylvania State University, 2014.
27. K. Leung, R. Lindstedt, and W. Jones, A simplified reaction mechanism for soot formation in nonpremixed flames, Combustion and Flame 87 (1991), pp. 289–305.
28. M. Frenklach, Method of moments with interpolative closure, Chemical Engineering Sci- ence 57 (2002), pp. 2229–2239.
29. S.P. Roy and D.C. Haworth, A systematic comparison of detailed soot models and gas- phase chemical mechanisms in laminar premixed flames, Combustion Science and Tech- nology 188 (2016), pp. 1021–1053.
30. N.J. Brown, K.L. Revzan, and M. Frenklach, Detailed kinetic modeling of soot forma- tion in ethylene/air mixtures reacting in a perfectly stirred reactor, Proceedings of the Combustion Institute 27 (1998), pp. 1573–1580.
31. J. Appel, H. Bockhorn, and M. Frenklach, Kinetic modeling of soot formation with detailed chemistry and physics: Laminar premixed flames of C_2 hydrocarbons, Combustion and Flame 121 (2000), pp. 122–136.
32. M. Frenklach, Reaction mechanism of soot formation in flames, Physical Chemistry Chemical Physics 4 (2002), pp. 2028–2037.
33. H. Wang, D.X. Du, C.J. Sung, and C.K. Law, Experiments and numerical simulation on soot formation in opposed-jet ethylene diffusion flames, Proceedings of the Combustion Institute 26 (1996), pp. 2359–2368.
34. M. Frenklach and H. Wang, Detailed mechanism and modeling of soot particle formation, in Soot Formation in Combustion: Mechanisms and Models, H. Bockhorn, ed., Springer- Verlag, New York, 1994.

35. S. Roy, Aerosol-dynamics-based soot modeling of flames, Ph.D. diss., The Pennsylvania State Universtiy, 2014.
36. R.P. Lindstedt and S.A. Louloudi, Joint-scalar transported PDF modeling of soot forma- tion and oxidation, Proc. Combust. Inst. 30 (2005), pp. 775–783.
37. G. Pal, A. Gupta, M.F. Modest, and D.C. Haworth, Comparison of accuracy and compu- tational expense of radiation models in simulation of non-premixed turbulent jet flames, Combustion and Flame 162 (2015), pp. 2487–2495.
38. A. Wang and M.F. Modest, Photon Monte Carlo simulation for radiative transfer in gaseous media represented by discrete particle fields, Journal of Heat Transfer 128 (2006), p. 1041.
39. L.S. Rothman, I.E. Gordon, R.J. Barber, H. Dothe, R.R. Gamache, A. Goldman, V.I. Perevalov, S.A. Tashkun, and J. Tennyson, HITEMP, the high-temperature molecular spectroscopic database, Journal of Quantitative Spectroscopy and Radiative Transfer 111 (2010), pp. 2139–2150.
40. H. Chang and T.T. Charalampopoulos, Determination of the wavelength dependence of refractive indices of flame soot, Proceedings of the Royal Society A: Mathematical, Phys- ical and Engineering Sciences 430 (1990), pp. 577–591.
41. A. Tuntomo, C.L. Tien, and S.H. Park, Optical constants of liquid hydrocarbon fuels, Combustion Science and Technology 84 (1992), pp. 133–140.
42. L. Dombrovsky, Thermal radiation from nonisothermal spherical particles (2000). Avail- able at doi:10.1615/thermopedia.000141.
43. L.A. Dombrovsky, S.S. Sazhin, S.V. Mikhalovsky, R. Wood, and M.R. Heikal, Spectral properties of diesel fuel droplets, Fuel 82 (2003), pp. 15–22.
44. P. Rosin, Laws governing the fineness of powdered coal, Journal of Institute of Fuel 7 (1933), pp. 29–36.
45. Engine Combustion Network, Pressure Based Ignition Delay. Available at https://ecn.sandia.gov/diesel-spray-combustion/experimental-diagnostics/ pressure-based-ignition-delay/.
46. O. Samimi Abianeh, M. Levins, and C.P. Chen, Pressure-Based Ignition Delay Times of Non-Premixed Turbulent Jet Flames Using Various Turbulence Models, in ASME Inter- nal Combustion Engine Division Fall Technical Conference, Vol. ICEF2016-9307. 2016, Available at doi:10.1115/ICEF2016-9307.
47. M. Bolla, D. Farrace, Y.M. Wright, K. Boulouchos, and E. Mastorakos, Influence of turbulence-chemistry interaction for n-heptane spray combustion under diesel engine con- ditions with emphasis on soot formation and oxidation, Combustion Theory and Modelling 18 (2014), pp. 330–360.
48. Y. Pei, E.R. Hawkes, and S. Kook, A comprehensive study of effects of mixing and chem- ical kinetic models on predictions of n-heptane jet ignitions with the PDF method, Flow, Turbulence and Combustion 91 (2013), pp. 249–280.
49. S. Bhattacharjee and D.C. Haworth, Simulations of transient n-heptane and n-dodecane spray flames under engine-relevant conditions using a transported PDF method, Combus- tion and Flame 160 (2013), pp. 2083–2102.
50. K.M. Mukut and S.P. Roy, A Sensitivity Study on Soot and NOx Formation in High Pressure Combustion System, in 2018 Spring Technical Meeting of Central States Section of the Combustion Institute, Minneapolis, MN. 2018.
51. Z.J. He, C. Chang, and C. Follen, NOx Emissions Performance and Correlation Equations for a Multipoint LDI Injector, in 53rd AIAA Aerospace Sciences Meeting, Kissimmee, FL. 2015.
52. N.J. Brown, L.A. Bastien, and P.N. Price, Transport properties for combustion modeling, Progress in Energy and Combustion Science 37 (2011), pp. 565–582.
53. F. Liu, H. Guo, G.J. Smallwood, and Ö.L. Gülder, Numerical modelling of soot forma- tion and oxidation in laminar coflow non-smoking and smoking ethylene diffusion flames, Combustion Theory and Modelling 7 (2003), pp. 301–315.
54. R. Salark, M. Shams, and R. Ebrahimi, Numerical simulation of soot formation in a turbulent diffusion flame: comparison among three soot formation models, Proc. IMechE Part C: J. Mechanical Engineering Science 226 (2012), pp. 1290–1301.

55. R. Mehta, D. Haworth, and M. Modest, An assessment of gas-phase reaction mechanisms and soot models for laminar atmospheric-pressure ethyleneair flames, Proceedings of the Combustion Institute 32 (2009), pp. 1327–1334.
56. S. Rigopoulos, Modelling of soot aerosol dynamics in turbulent flow, Flow, Turbulence and Combustion 103 (2019), pp. 565–604.
57. E. Cenker, K. Kondo, G. Bruneaux, T. Dreier, T. Aizawa, and C. Schulz, Assessment of soot particle-size imaging with LII at diesel engine conditions, Applied Physics B: Lasers and Optics 119 (2015), pp. 765–776.
58. J. Towns, T. Cockerill, M. Dahan, I. Foster, K. Gaither, A. Grimshaw, V. Hazlewood, S. Lathrop, D. Lifka, G. Peterson, R. Roskies, J.R. Scott, and N. Wilkins-Diehr, XSEDE: Accelerating scientific discovery, Computing in Science & Engineering 16 (2014), pp. 62– 74.
59. S.P. Roy, P.G. Arias, V. Lecoustre, H.G. Im, D.C. Haworth, and A. Trouvé, Development of High Fidelity Soot Aerosol Dynamics Models using Method of Moments with Interpola- tive Closure, Aerosol Science and Technology 48 (2014), pp. 379–391.

Published version can be found at DOI:10.1080/13647830.2020.1721561
Corresponding Author: S. P. Roy. Email: somesh.roy@marquette.edu

Table 1.: Summery of numerical models and parameters used in the current study

Physical Process	**Formulation**	**Models**	**Co-efficient Values**
Turbulence	URANS [18]	$k-\epsilon$ model	$C_{\epsilon 1}$=1.55[20], C_{μ}=0.09, C_{E2}=1.92, $C_{\epsilon 3}$=-0.33, σ_k=1.00, σ_{ϵ}=1.30
Combustion		Partially Stirred Reactor (PaSR)	C_{mix} = 0.1
Fuel Spray	Stochastic Lagrangian Parcel [21]	Blob atomization and Reitz-Diwakar secondary break-up model[21]	LBU=1.0, C_{bag}=6.0, C_b=0.785, C_{strip}=0.5, C_s = 9.00
Gas Phase Thermo-chemistry	Ideal Gas Mixture		54 species n-dodecane [23] (augmented with thermal NO)
Soot		Semi-empirical two-equation model [27], and MOMIC [28, 59]	
Initial k and ϵ			k = 0.25 m_2/s_2 [8] and ϵ = 41 m_2/s_3 [8]

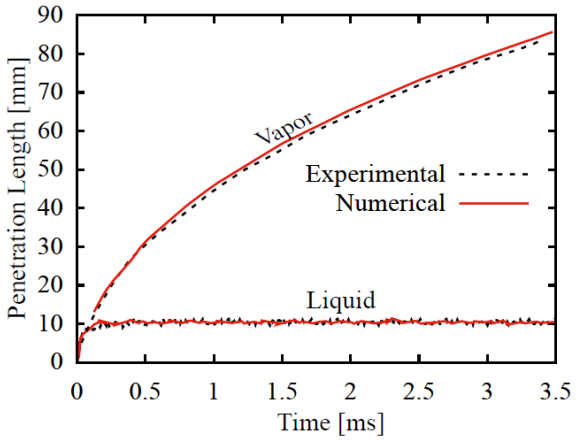

Figure 1.: Comparison of numerically and experimentally obtained liquid and vapor penetration lengths in 0% O_2 case.

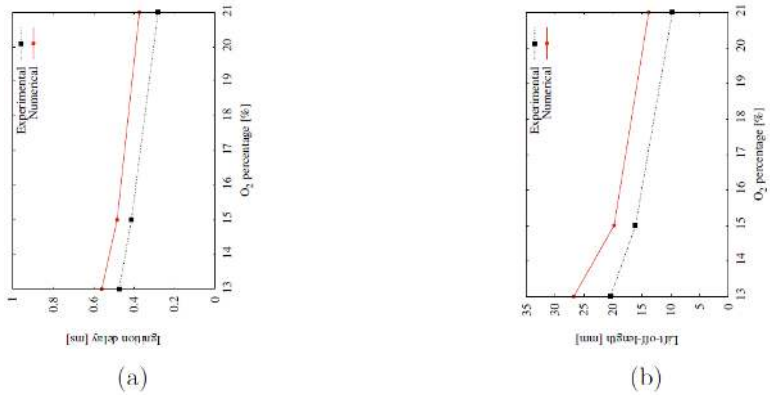

Figure 2.: Comparison between experimental and numerical (a) ignition delay (ID) and (b) lift-off-length (LOL) with change in O_2 % in the ambient gases.

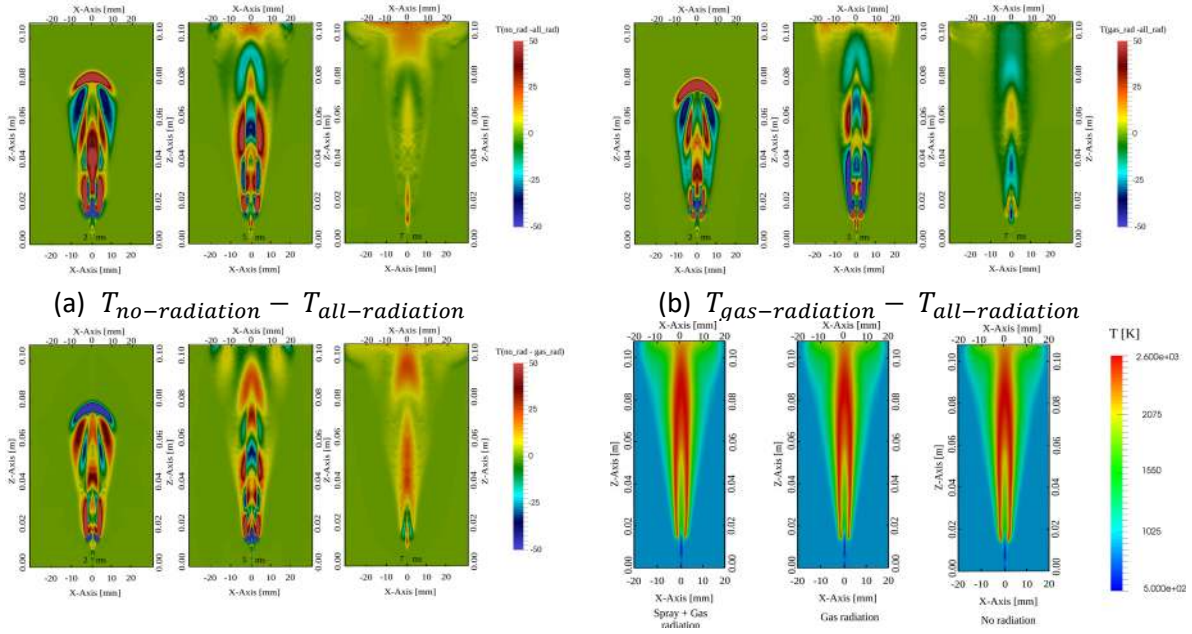

(a) $T_{no-radiation} - T_{all-radiation}$

(b) $T_{gas-radiation} - T_{all-radiation}$

(c) $T_{no-radiation} - T_{gas-radiation}$

(d) Temperature contours with radiation

Figure 3.: Temporal evolution of temperature difference due to (a) all (spray and gas-phase) radiation, (b) spray-phase radiation only, (c) gas-phase radiation only and (d) temperature contour with and without radiation at 5 ms for 21% O_2 percentage.

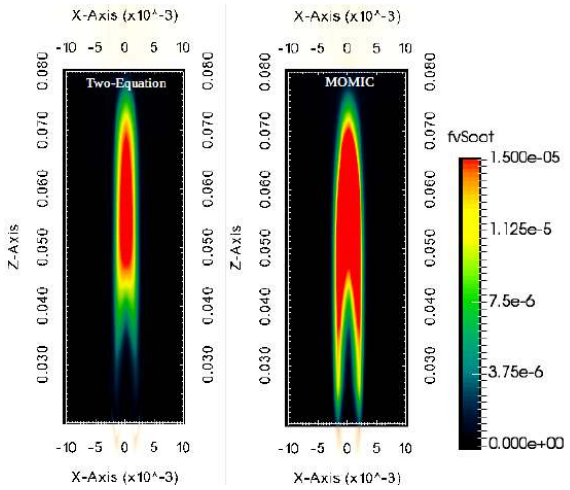

Figure 4.: Soot volume fraction contours with different soot models for 21% O_2 case at 5 ms.

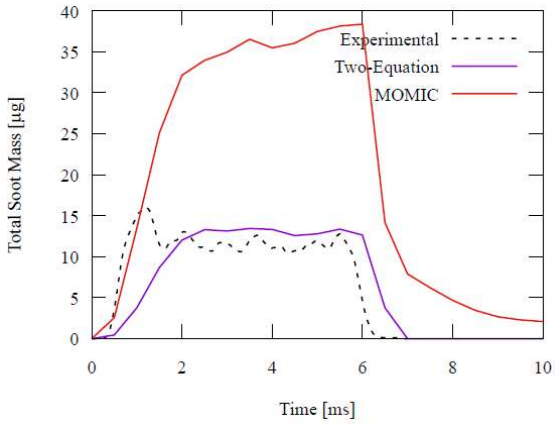

Figure 5.: Evolution of soot with time within the experimental field of view with different soot models for 21% O_2 case

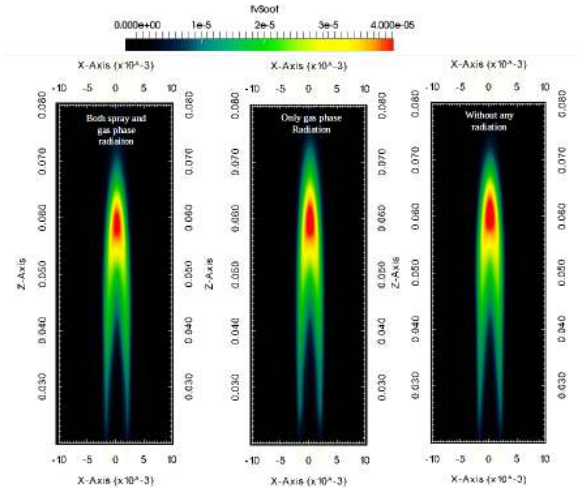

Figure 6.: Soot volume fraction contours with and without radiation for 21% O_2 case with MOMIC at 5 ms

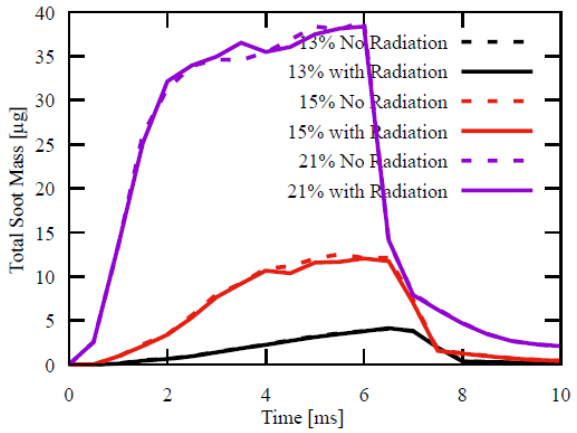

Figure 7.: Evolution of total soot mass with time for different O_2 percentage configurations with MOMIC

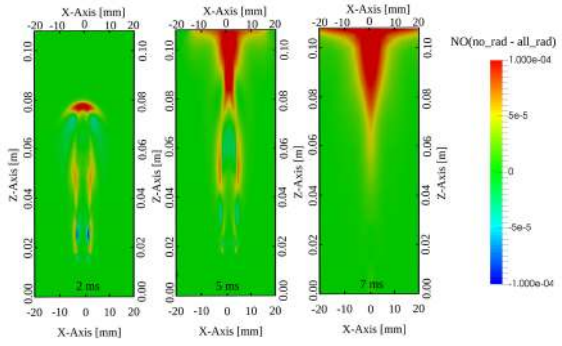

(a) $NO_{no-radiation} - NO_{all-radiation}$

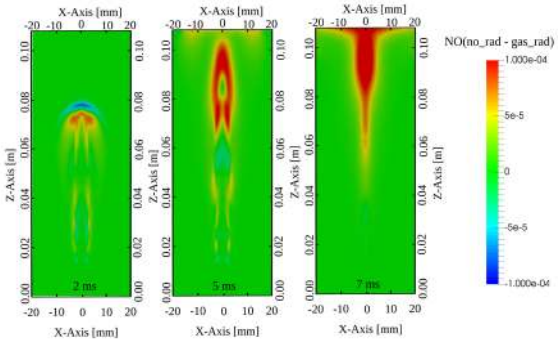

(b) $NO_{no-radiation} - NO_{gas-radiation}$

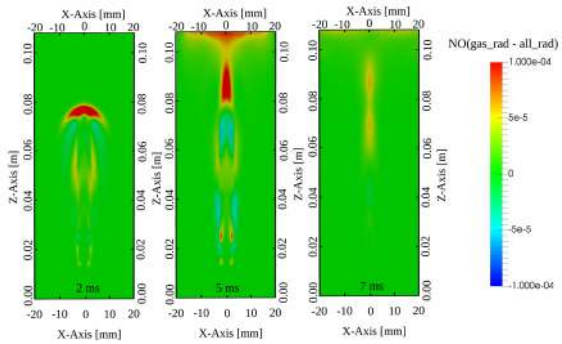

(c) $NO_{gas-radiation} - NO_{all-radiation}$

Figure 8.: Change of NO mass fraction with time due to (a) all (spray and gas) radiation, (b) gas-phase radiation only (c) spray-radiation only at 21% O_2 case.

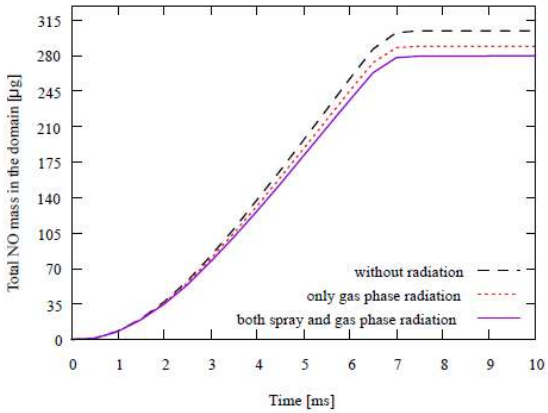

Figure 9.: Variation of total NO mass in the simulation domain with and without radiation at 21% O_2 case

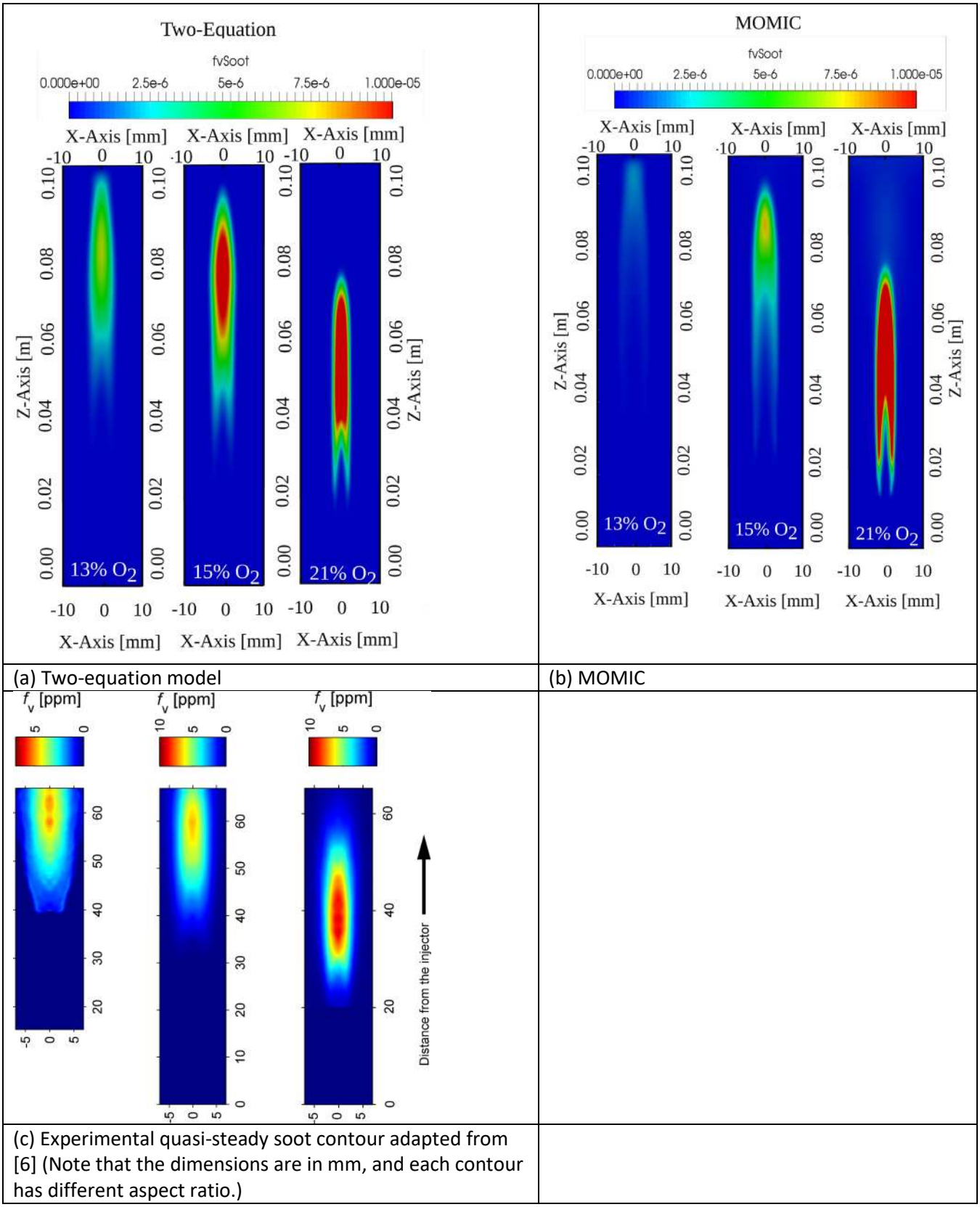

(a) Two-equation model

(b) MOMIC

(c) Experimental quasi-steady soot contour adapted from [6] (Note that the dimensions are in mm, and each contour has different aspect ratio.)

Figure 10.: Soot volume fraction contours across different O_2 percentages using (a) two-equation soot model, (b) MOMIC at 5 ms and (c) experimental quasi-steady soot volume fraction (adapted from [6]).

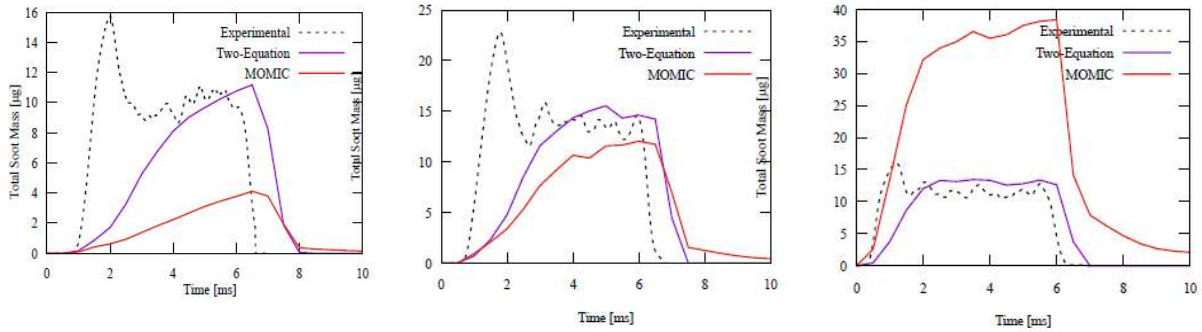

(a) 13% O_2 (b) 15% O_2 (c) 21% O_2

Figure 11.: Effect of O_2 quantity in the ambient mixture and soot models on global soot formation characteristics in the experimental field of view

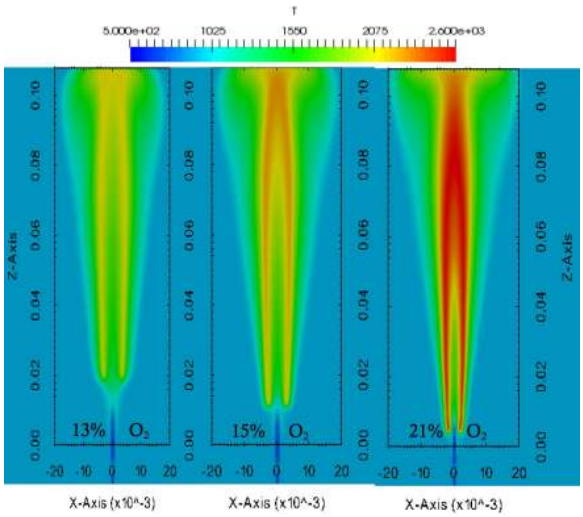

Figure 12.: Temperature contours for different O_2 percentage cases at 5 ms

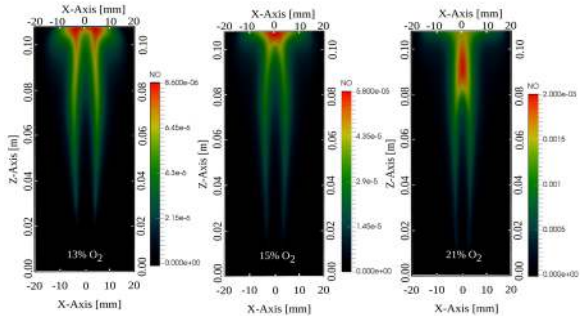

Figure 13.: NO mass fraction contours for different O_2 percentage cases at 5 ms

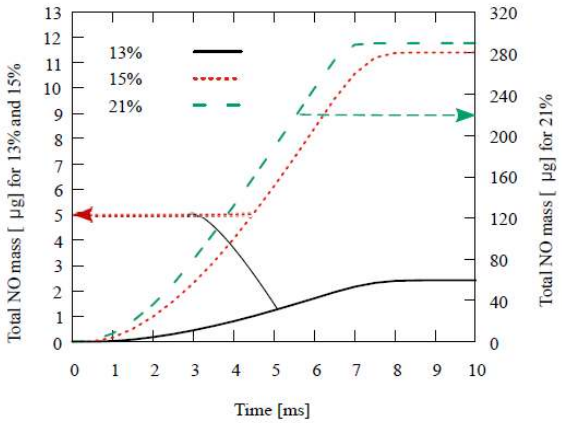

Figure 14.: Effect of O_2 percentage in the ambient mixture on the total NO mass produced in the simulation domain (13% & 15% in left axis and 21% in right axis)

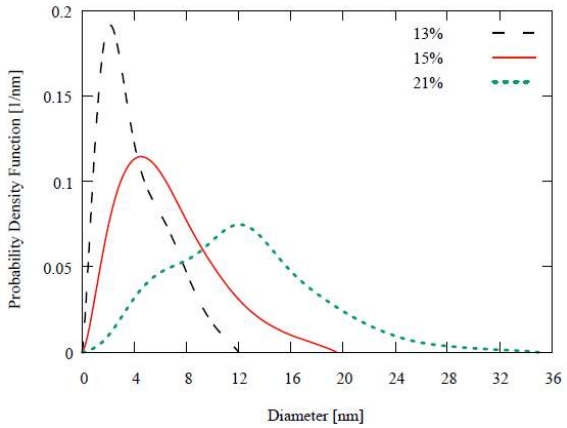

Figure 15.: PDF of soot diameter with different initial O_2 configurations at 5 ms.

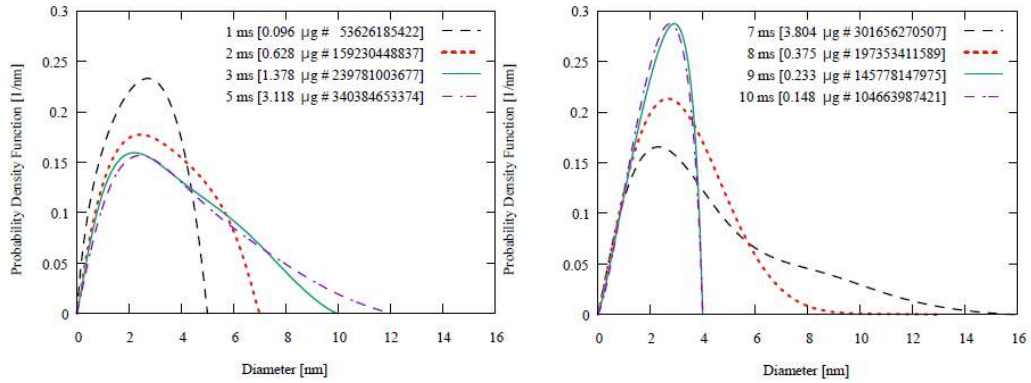

(a) During the spray injection (b) After the end of spray injection

Figure 16.: Evolution of PDF of soot diameter with time at 13% O_2 case; (a) during injection, (b) after the end of injection

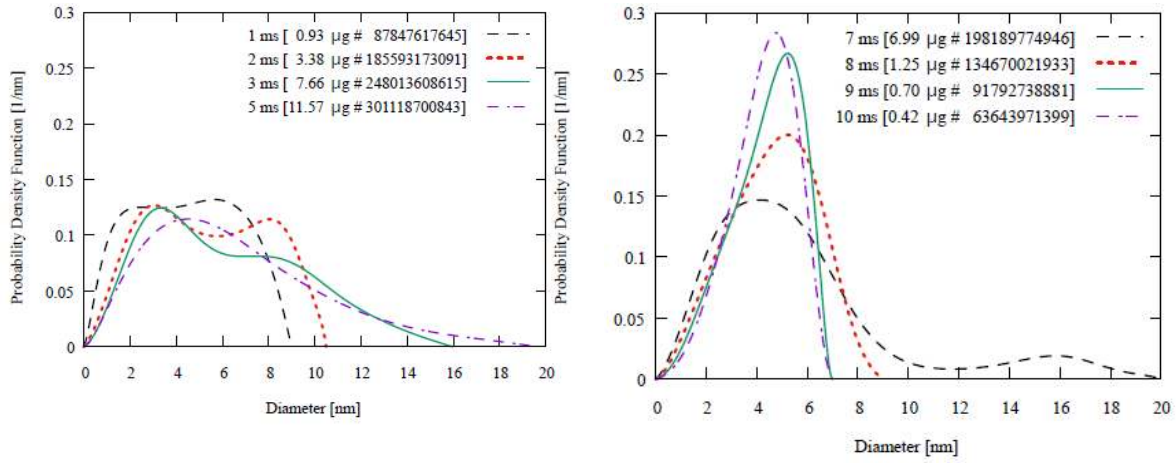

(a) During the spray injection (b) After the end of spray injection

Figure 17.: Evolution of PDF of soot diameter with time at 15% O_2 case; (a) during injection, (b) after the end of injection

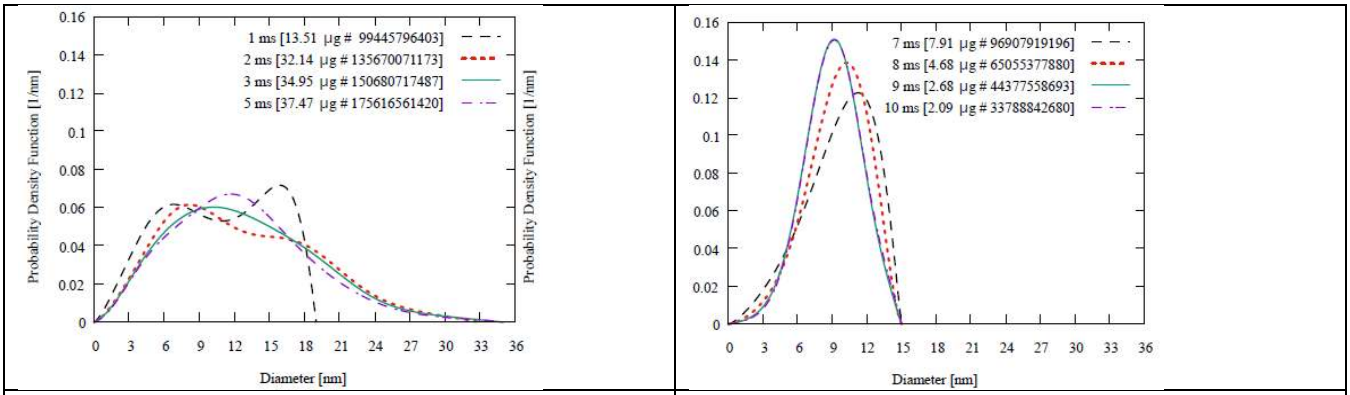

(a) During the spray injection (b) After the end of spray injection

Figure 18.: Evolution of PDF of soot diameter with time at 21% O_2 case; (a) during injection, (b) after the end of injection

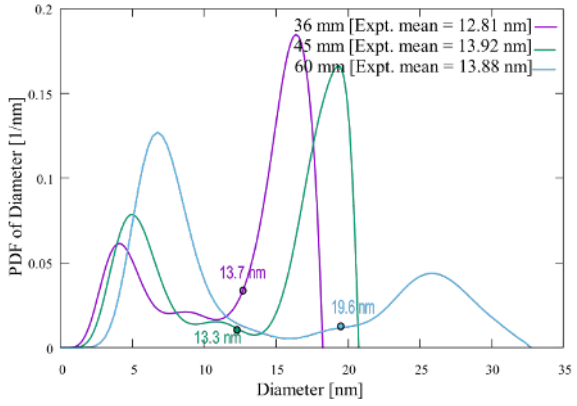

Figure 19.: Planar-averaged PDF of soot diameter for 21% O_2 configuration at different axial locations. The dots represent the computed mean diameter. The experimental mean diameter [57] is noted in the legends.